# nature communications



**Article** 

https://doi.org/10.1038/s41467-025-65772-2

# East Siberian ice wedges recording dust transport variability during the Late Pleistocene

Received: 16 January 2025

Accepted: 23 October 2025

Published online: 10 November 2025



Soyeon Kim <sup>1</sup>, Hyunwoo Lee <sup>1</sup> □, Jeongmin Kim<sup>2</sup>, Yuyoung Lee<sup>2</sup>, Jeong-Heon Choi <sup>2</sup>, Mi Jung Lee<sup>3</sup>, Ui-Jin Kwon <sup>1</sup>, Go Iwahana <sup>4</sup>, Thomas Opel <sup>5</sup>, Hanno Meyer <sup>5</sup>, Sebastian Wetterich <sup>5,6</sup>, Alexander Fedorov <sup>7</sup> & Jinho Ahn <sup>1</sup>

During the Late Pleistocene, a severely cold and dry climate strengthened dust production across the Northern Hemisphere. Despite many studies examining aridification and dust production, there is a lack of understanding about dust transportation during global climate variability. Long-range transported (LRT) dust can be traced by comparing global geochemical signatures and constraining provenance relationships. Here we report rare earth element abundances and strontium, neodymium, and oxygen isotope compositions of inorganic substances in ice wedges from Batagay and Central Yakutia (Cyuie and Churapcha), which comprise Yedoma deposits that formed in unglaciated Beringia. Distinct geochemical properties reflect differences between local and LRT dust contributions. Particles in the Batagay ice wedges show higher similarities to Chinese aeolian deposits, while those in Central Yakutia indicate stronger local input. These provenance constraints highlight variability in atmospheric circulation transporting dust to the Arctic during the Late Pleistocene, linking climate changes to aerosol distribution.

Mineral dust in the atmosphere, one of the key components of the climate system, can be used as an indicator to examine climate change. It is transported by the Earth's wind regime, affected by both the regional and large-scale climate system<sup>1</sup>. Dust in proximal regions is mainly carried by near-surface winds via creeping and saltation<sup>2,3</sup>, while long-range transport (LRT) from distal regions is largely driven by synoptic-scale atmospheric circulation<sup>3,4</sup>. The frequency and intensity of such LRT events may be modulated by millennial-scale climate oscillations<sup>5</sup>. Additionally, atmospheric dust directly absorbs and scatters radiation and indirectly modifies the properties of clouds, affecting Earth's climate systems<sup>6,7</sup>. Dust radiative forcing also makes an important contribution to polar amplification<sup>8</sup>. Thus, investigating

provenance, distribution, and transport of dust is crucial to understanding dust-climate linkages and how atmospheric conditions respond to climate change.

During the last glacial period, dust production and deposition were greatly enhanced  $^{9,10}$ . Dust is recorded in many deposits, particularly loess, which can incorporate both LRT dust and locally derived material  $^9$ . Loess is primarily composed of silt-sized particles (2–63  $\mu m$ ), but often incorporates a significant fraction finer than 10  $\mu m$ , potentially reflecting background dust transported hundreds to thousands of kilometers by westerlies  $^{11,12}$ . Accordingly, loess and loess-like deposits serve as valuable archives of past dust dynamics. Located across central and northern Siberia, Yakutia is one of the

<sup>1</sup>School of Earth and Environmental Sciences, Seoul National University, Seoul, Republic of Korea. <sup>2</sup>Research Center of Earth and Environmental Sciences, Korea Basic Science Institute, Ochang, Chungcheongbuk-do, Republic of Korea. <sup>3</sup>Division of Glacier and Earth Sciences, Korea Polar Research Institute, Incheon, Republic of Korea. <sup>4</sup>International Arctic Research Center, University of Alaska, Fairbanks, AK, USA. <sup>5</sup>Alfred Wegener Institute, Helmholtz Centre for Polar and Marine Research, Potsdam and Bremerhaven, Germany. <sup>6</sup>Institute of Geography, Technische Universität Dresden, Dresden, Germany. <sup>7</sup>Melnikov Permafrost Institute, Siberian Branch RAS, Novosibirsk, Russia. Ee-mail: lhw615@snu.ac.kr

major regions where loess is distributed<sup>11,13,14</sup>, and there is a special type of loess-like deposits called Yedoma (Fig. 1; Supplementary Fig. 1). Yedoma, or ice complex, is a silt-dominated ice-rich syngenetic permafrost with massive ice wedges, which developed across Beringia during the Late Pleistocene<sup>11,15,16</sup>. Although Yedoma in Alaska (i.e., eastern Beringia) has been considered to be aeolian-processed deposits since ref. 17, the depositional processes of Yedoma in Siberia (i.e., western Beringia) remain debated<sup>13,15,16</sup>. Because Siberia

lies at the interface between major mid-latitude dust sources and the Arctic, understanding the provenance and transport mechanisms of Yedoma source material is crucial for reconstructing past atmospheric dust circulation and its climatic implications.

Syngenetic ice wedges, widely distributed in northeastern Siberia, grew during permafrost formation and accommodated significant amounts of sediment<sup>18</sup>, recording paleoclimate and paleoenvironment conditions during permafrost development. A substantial portion of

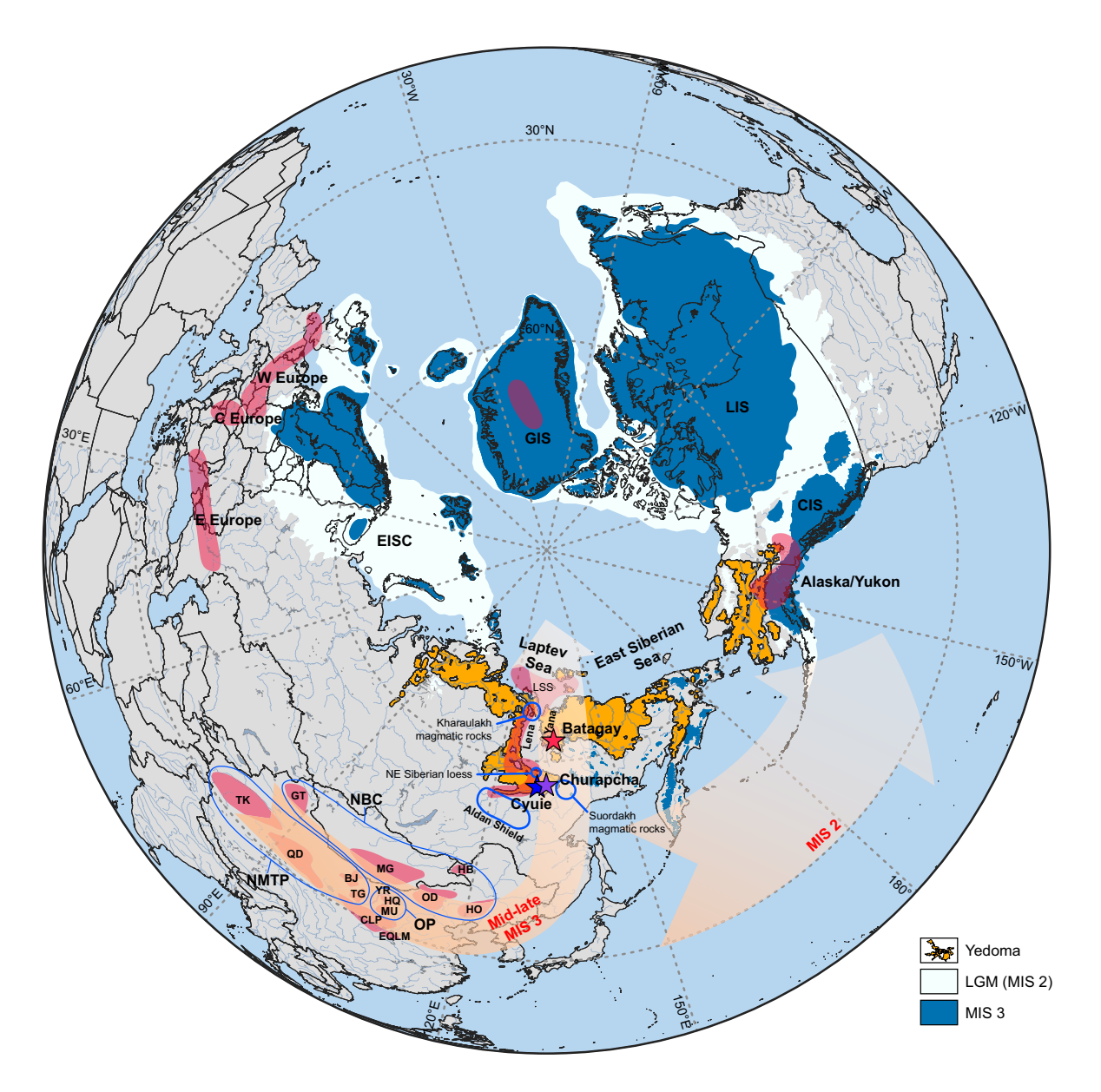


**Fig. 1** | **Map of the study area.** Yedoma deposits (yellow-filled areas; from refs. 65,66), possible source areas (PSA; red-shaded and blue-outlined), and schematic dust transport paths (orange arrows) during the Late Pleistocene are shown. Arrows represent episodic events likely more frequent during their respective periods and do not depict mean climatology. Red, blue, and purple stars indicate the sampling locations of the Batagay, Cyuie, and Churapcha ice wedges, respectively. Reconstructed ice-sheet extents (Eurasian Ice Sheet Complex, EISC; Greenland Ice Sheet, GIS; Laurentide ice sheet, LIS; Cordilleran Ice Sheet, CIS) are shown for Marine Isotope Stages (MIS) 3 and the Last Glacial Maximum (LGM; MIS 2) as derived from refs. 60,61; see Methods for details. Major PSAs include the Taklimakan Desert (TK), Qaidam Basin (QD), Badain Jaran Desert (BJ), and Tengger Desert (TG) along the northern margin of the Tibetan Plateau (NMTP); the Yellow River (YR), Hobq Desert (HQ), and Mu Us Desert (MU) in the Ordos Plateau (OP); and the Mongolian Gobi

(MG). Additional PSAs include the Gurbantunggut Desert (GT), Onqin Daga sandy land (OD), Hunlun Buir sandy land (HB), and Horqin sandy land (HO) along the northern boundary of China (NBC), as well as the Chinese Loess Plateau (CLP), Eastern Qinling Mountains (EQLM), Alaskan-Yukon loess and dust, Greenland glacial dust, and Western (W), Central (C), and Eastern (E) European loess. For comparison with potential local sources, we also include suspended particulate matter (SPM) from the Lena and Yana Rivers, Laptev Sea sediments (LSS), northeastern (NE) Siberian loess, Aldan Shield lamproites, and mafic magmatic rocks from the eastern margin of the Siberian Craton (Kharaulakh and Suordakh events). Base map includes rivers from Natural Earth (public domain). National boundaries are based on the TM World Borders Dataset 0.3 (available at https://larmarange.github.io/prevR/reference/TMWorldBorders.html), licensed under CC BY-SA 3.0 (https://creativecommons.org/licenses/by-sa/3.0/).

the Yedoma deposits has been lost during post-depositional permafrost degradation, changing the permafrost environment since the Pleistocene-Holocene transition<sup>19,20</sup>. Nevertheless, well-preserved syngenetic ice wedges without thaw evidence are considered to retain original materials and geochemical signatures, which were implemented during Yedoma formation<sup>21-23</sup>. To elucidate the origin and transport of Yedoma sediments during the Late Pleistocene, we sampled such well-preserved syngenetic ice wedges without any thawrelated disturbance from Batagay (upper ice complex, UIC) and Central Yakutia (Cyuie and Churapcha) (Supplementary Notes; Supplementary Figs. 2, 3; Supplementary Table 1). Formation ages of the ice wedges studied in the middle part of the Batagay UIC (~60–27 ka; ref. 24) fall within the middle to late (mid-late) Marine Isotope Stages (MIS) 3 (~45-30 ka), based on newly available radiocarbon ages (see Methods; Supplementary Notes; Supplementary Table 2), which corresponds to the period before the Last Glacial Maximum (LGM). In contrast, the Central Yakutia ice wedges formed in early to middle MIS 2 (~21-18 ka; refs. 21,22), representing the LGM period.

In this study, we constrain the provenance and transport pathways of inorganic solid particles preserved in syngenetic ice wedges from Batagay and Central Yakutia by measuring trace element concentrations, particularly rare earth elements (REE), and isotope compositions of Sr, Nd, and O, which have been widely used to trace provenances for various types of materials (e.g., rock, sediment, and dust; refs. 1,25–27). Formed mainly by snow compaction and hoar frost accretion<sup>22,23</sup>, rather than surface water infiltration, our ice wedge samples effectively trap atmospheric input and are expected to preserve atmospheric dust signals. Unlike host sediments, well-preserved ice wedge infill is less affected by redeposition and sediment reworking, and thus can more directly record atmospheric deposition during ice wedge growth. Together, these datasets allow us to evaluate the relative contributions of local versus LRT sources during the mid-late MIS 3 (Batagay) and the LGM (MIS 2; Central Yakutia).

### Results

#### **Grain-size distributions and trace element systematics**

The possibility of containing the LRT dust in both regions is suggested by the bimodal to polymodal grain-size distributions, indicative of a polygenetic origin (Supplementary Notes; Supplementary Fig. 4; Supplementary Data 1; refs. 12,28). Alongside a dominant silt-sized peak (10–80  $\mu m$  range), all samples display a secondary mode or shoulder around 1  $\mu m$ , consistent with the fine-grained LRT dust. Because REE, Sr isotope, and quartz oxygen isotope compositions can be grain-size dependent  $^{25,26,29}$ , we therefore analyze size-separated fractions (see Methods).

REE concentrations varied across grain-size fractions but did not exhibit any systematic correlation with particle size (Supplementary Fig. 5; Supplementary Data 2). Differences between sample groups are more prominent than those among grain-size fractions, indicating that the REE concentrations are mainly controlled by provenance rather than grain-size effects. To compare the geochemical compositions of all samples and possible source areas (PSAs), Fig. 2 and Supplementary Fig. 6 present selected element ratios, including REE and other trace elements. These data are normalized to post-Archean Australian shale (PAAS; ref. 30). The element ratios used in these binary plots have been suggested as useful particle size-independent provenance tracers<sup>25</sup>.

The binary plots suggest that our samples represent mixtures of LRT dust from the Chinese sources and locally derived material, with varying proportions (Fig. 2; Supplementary Fig. 6). The Batagay samples overlap closely with the Ordos Plateau (OP) field, suggesting a relatively stronger input from Chinese dust. In contrast, the Central Yakutia samples fall between the fields of the Lena and Yana River suspended particulate matter (SPM) and the northern China aeolian deposits, probably the OP, suggesting a mixture of regional input and distal dust sources. Europium anomalies (Eu/Eu\*) also distinguish the

two groups (Supplementary Notes; Supplementary Fig. 5): the Batagay samples overlap with the OP to the northern margin of the Tibetan Plateau (NMTP) fields, whereas the Central Yakutia samples align more closely with the Lena and Yana SPM (Fig. 2c, d; Supplementary Fig. 6a–e). In detail, the Lena River SPM systematically shifts toward the Aldan Shield lamproites across all element ratios. The Central Yakutia samples show a similar deviation, trending toward both the Lena River SPM and the Aldan Shield lamproites, likely demonstrating a substantial contribution from this crystalline lithology of the Aldan Shield.

#### Strontium and neodymium isotopes

The measured  $^{87}\text{Sr}/^{86}\text{Sr}$  ratios of bulk ice wedge sediments range from 0.715784 to 0.717100 in Batagay and from 0.716610 to 0.717291 in Central Yakutia (Fig. 3; Supplementary Data 3). The fine fractions (<10 and <5  $\mu m$ ) show higher ratios, ranging from 0.719567 to 0.722099 in Batagay and from 0.720124 to 0.721181 in Central Yakutia, indicating a grain-size effect with increasing  $^{87}\text{Sr}/^{86}\text{Sr}$  toward the fine fractions. In contrast,  $\epsilon_{Nd}(0)$  values show little evidence of grain-size effects but display clear regional differences. Bulk  $\epsilon_{Nd}(0)$  values from the Batagay samples (–8.8 to –8.5) are higher than those from the Central Yakutia samples (–18.3 to –16.3), and the fine fractions show the same contrast (–8.2 to –7.9 in Batagay and –14.7 to –14.3 in Central Yakutia), highlighting the distinct provenance signals between the two sites.

The Batagay values appear near the isotope range of the Greenland glacial dust and are plotted between the ranges of Mongolian Gobi Desert (MG), northern boundary of China (NBC), Chinese Loess Plateau (CLP), and the NMTP (Fig. 3). This similarity in radiogenic isotopes suggests that our samples may share a common East Asian provenance with the Greenland glacial dust. Numerous studies have reported that dust in the Greenland ice cores originated from major dust-emitting sources in East Asia (e.g., CLP, MG, and the Taklimakan Desert, TK) during the last glacial period<sup>31-33</sup>. Although dust of European origin has also been reported in Greenland, and Sr-Nd isotopes alone are insufficient to distinguish between European and Asian sources<sup>34</sup>, geographical distance makes it more plausible that atmospheric dust deposited in our study area originated from East Asia.

Bulk Central Yakutia samples overlap with the isotopic range of Alaskan loess, and the  $\epsilon_{Nd}(0)$  values overlap with those of Aldan Shield lamproites (Fig. 3). Although direct comparison of Sr isotopes is complicated by grain-size effects and by the use of whole-rock lamproite values²6.35, the  $\epsilon_{Nd}(0)$  overlap suggests a contribution from the Aldan Shield-derived material. The more radiogenic  $^{87}\text{Sr}/^{86}\text{Sr}$  in the Central Yakutia samples relative to the lamproites can be attributed to grain-size partitioning²6. However, the fine fractions (<10 and <5  $\mu$ m) shift for both Sr and Nd isotopes toward the fields of the Eastern Qinling Mountains (EQLM) and OP, suggesting additional contributions of Chinese dust, consistent with mixing signatures inferred from REE ratios (Fig. 2).

Although the reported <sup>87</sup>Sr/<sup>86</sup>Sr values for the Lena and Yana River SPM (0.716624 to 0.717728 for the Lena; 0.713647 to 0.716892 for the Yana and its tributary; ref. 36) are similar to those of our samples, Nd isotopes for these rivers are scarce. We alternatively compare our dataset with the Laptev Sea sediments (LSS) and northeastern (NE) Siberian loess as more integrative local references (Fig. 3). The LSS cannot be regarded as a single definitive local endmember, because the LSS represents a mixture of sediments derived from diverse sources, including coastal erosion and river discharge, and because riverine SPM draining limited watersheds can have different chemical compositions<sup>37,38</sup>. Nonetheless, the isotopic similarity between LSS and all samples suggests that local sources likely contributed to the ice wedge sediments. Similarly, NE Siberian loess exhibits Sr isotopes comparable to our samples at equivalent size fractions (<5 μm).

However, NE Siberian loess shows Nd isotope compositions distinct from the samples. This  $\varepsilon_{Nd}(0)$  discrepancy indicates that the Nd systematics require additional components, consistent with mixing

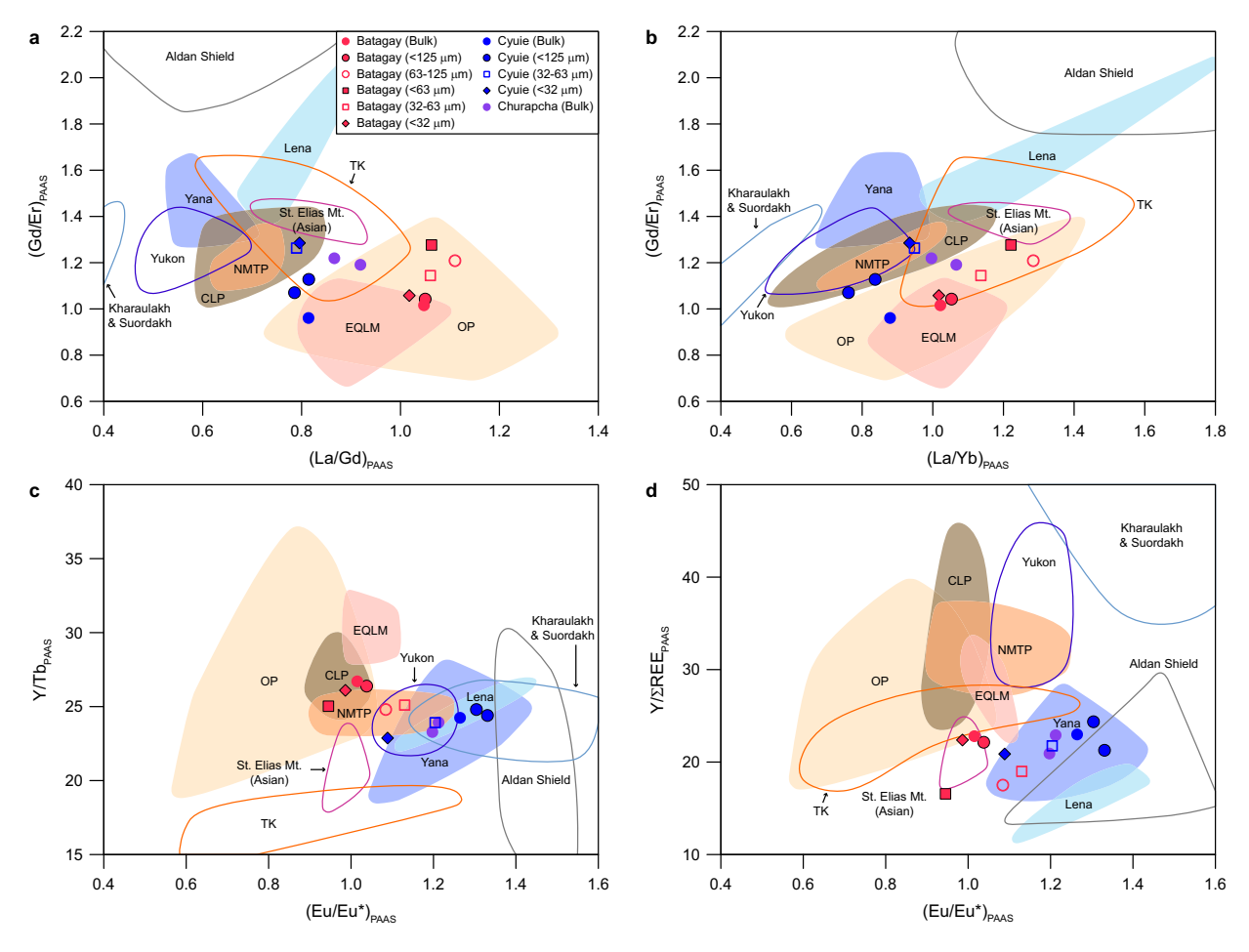


Fig. 2 | Bivariate plots of selected element ratios. a  $(Gd/Er)_{PAAS}$  vs  $(La/Gd)_{PAAS}$ . b  $(Gd/Er)_{PAAS}$  vs  $(La/Yb)_{PAAS}$ . c  $Y/Tb_{PAAS}$  vs  $(Eu/Eu^*)_{PAAS}$ . d  $Y/\sum_{REE_{PAAS}}$  vs  $(Eu/Eu^*)_{PAAS}$ . The subscript PAAS indicates that element concentrations were normalized to post-Archean Australian shale  $^{30}$ . Red, blue, and purple symbols denote ice wedge sediments from Batagay, Cyuie, and Churapcha, respectively, covering both bulk and grain-size fractions. Possible source areas (PSAs) are shown as shaded or outlined fields, including surface mud crusts from the northern margin of the Tibetan Plateau (NMTP), sands from the Taklimakan Desert (TK), sands from the

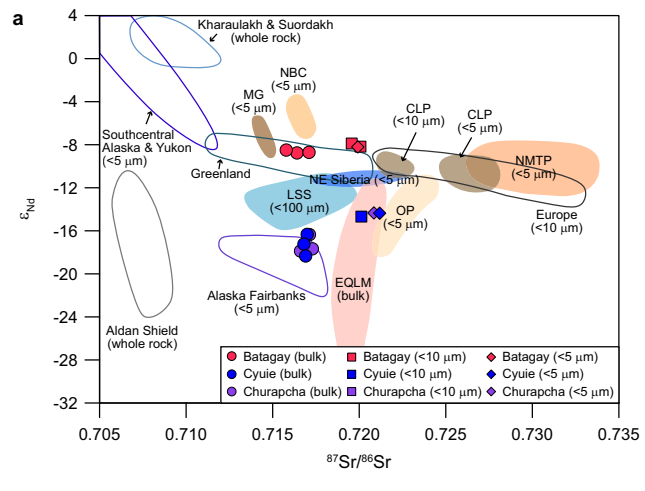
Ordos Plateau (OP), loess from the Eastern Qinling Mountains (EQLM), loess and paleosols from the Chinese Loess Plateau (CLP), suspended particulate matter (SPM) from the Lena and Yana Rivers, and local lithologies such as Aldan Shield lamproites and Kharaulakh-Suordakh magmatic rocks, together with comparable datasets from Yukon loess and St. Elias Mountain dust of probable Asian origin. Data sources and information for PSAs and comparable regions are provided in Supplementary Data 2.

between local lithologies and LRT dust. Indeed, all samples fall within the mixing field defined by several PSAs (Fig. 3b). The Batagay samples cannot be explained solely by local lithologies such as the Kharaulakh-Suordakh volcanic rocks or Aldan Shield lamproites. Because those reference values are based on whole-rock measurements and therefore not directly comparable to the fine sediment fractions, we treat them as bounding constraints on the local compositional range. The Batagay values are consistent with mixing between a set of hypothetical local endmembers (reflecting Kharaulakh-Suordakh and Aldan Shield contributions) and the OP-NMTP mixing endmembers (red dotted lines in Fig. 3b). For Central Yakutia, mixing trajectories between the OP-NMTP mixing endmembers and a local endmember defined by the bulk samples can explain the observed shift toward finer fractions (blue dotted lines in Fig. 3b). The bulk Central Yakutia compositions are taken as an approximation of the local source, showing Aldan Shield-like  $\varepsilon_{Nd}(0)$  values and elevated  ${}^{87}\text{Sr}/{}^{86}\text{Sr}$  compared to lamproites. Taken together, these results suggest that both study sites may contain LRT dust from the OP and NMTP in addition to local material. This interpretation is broadly consistent with the REE-based evidence (Fig. 2), which also points to contributions from Chinese PSAs. We note, however, that REE and Sr-Nd isotope signatures can be influenced by distinct grain-size and mineralogical fractions, which

may account for the minor discrepancies observed between the two provenance signals. The REE data suggest OP as the dominant source (Fig. 2), whereas the Sr-Nd isotopes imply mixing with additional components (Fig. 3).

#### Quartz oxygen isotopes

Oxygen isotope compositions of quartz grains are effective in differentiating distinct provenances in well-mixed aeolian dust<sup>1</sup>. Since δ<sup>18</sup>O values of aeolian quartz are influenced by grain-size effects with lowtemperature microcrystalline quartz<sup>29</sup>, we report grain-by-grain isotopic compositions subdivided by grain-size to avoid such effects (see Methods; Fig. 4; Supplementary Data 4). The  $\delta^{18}O$  (vs V-SMOW) distributions of all grain-size fractions are generally characterized by two dominant isotope ranges, around +10% and +15% (Fig. 4). The overall distributions differ between Batagay and Central Yakutia, and these differences are confirmed by statistical analyses (see Fig. 4 caption). For three coarser fractions (>32 μm), the Batagay samples show relatively wide peak areas from +10 to +20%, while the Central Yakutia samples have primary peaks at +10% and secondary peaks around +15%. The finest fractions (<32 µm) exhibit broad distributions at all sites, suggesting the mixing of various grain provenances. In particular, the dominant peak areas for the finest fraction of the Batagay



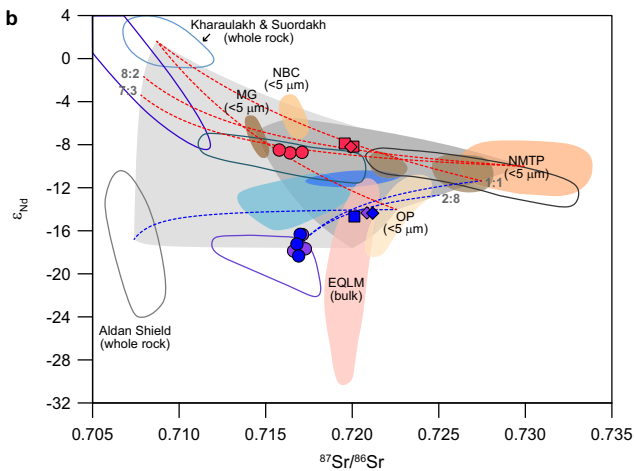
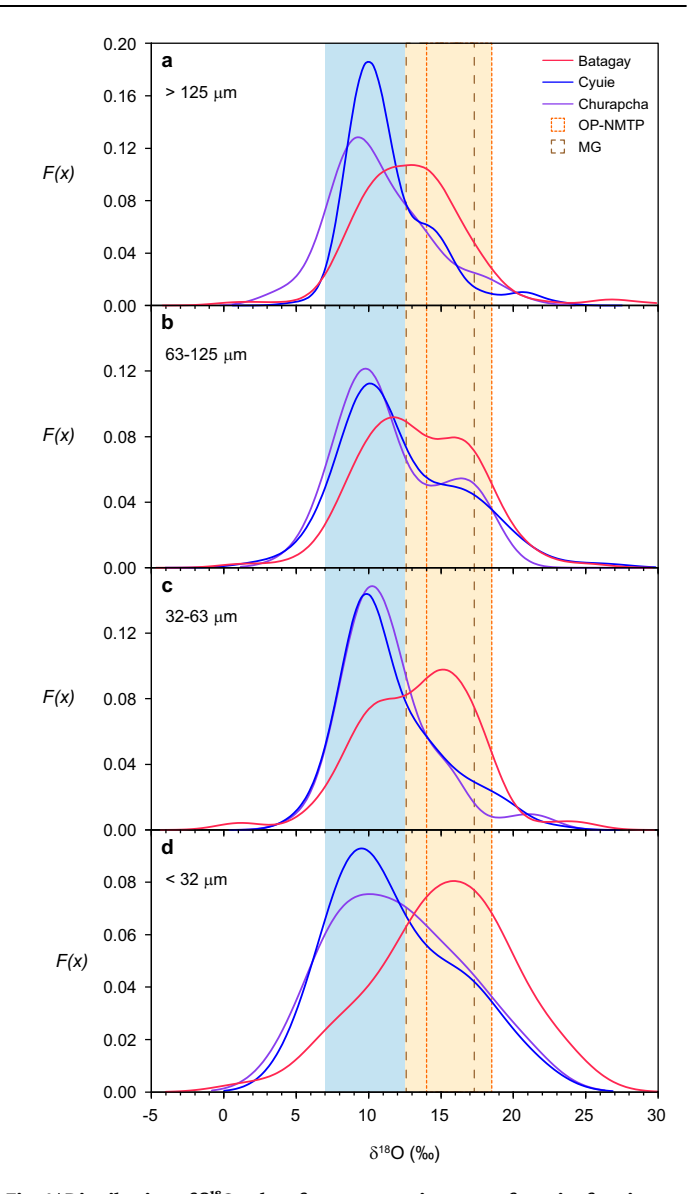


Fig. 3 | Sr-Nd isotope compositions. a  $\epsilon_{Nd}$  vs  $^{87}$ Sr/ $^{86}$ Sr for ice wedge sediments from Batagay, Cyuie, and Churapcha, shown for bulk samples (dominant grain-size modes of 50-80 μm, 20-70 μm, and 10-60 μm, respectively; see Supplementary Notes and Supplementary Fig. 4) as well as fine fractions (<10 and <5 μm), compared with possible source areas (PSAs) and reference datasets shown as shaded or outlined fields.  $\varepsilon_{Nd}$  denotes present-day values,  $\varepsilon_{Nd}(0)$ , calculated as  $[(^{143}Nd/^{144}Nd)_{sample}/(^{143}Nd/^{144}Nd)_{CHUR} - 1] \times 10^4$ , with  $(^{143}Nd/^{144}Nd)_{CHUR} = 0.512638$ (CHUR = chondritic uniform reservoir). PSA fields include sands from the Mongolian Gobi (MG), northern boundary of China (NBC), Ordos Plateau (OP) and northern margin of the Tibetan Plateau (NMTP): loess from the Chinese Loess Plateau (CLP), Eastern Qinling Mountains (EQLM) and northeastern (NE) Siberia; Laptev Sea sediments (LSS); and local lithologies (Aldan Shield and Kharaulakh-Suordakh volcanic rocks, whole-rock data). Additional datasets comprise European loess, Greenland dust, and Alaskan and Yukon loess. Data sources and information are given in Supplementary Data 3. b Same plot showing mixing relationships among PSAs. Dark-gray shading indicates the isotopic mixing range among the Chinese PSAs, whereas light-gray shading represents the extended mixing field between the Chinese PSAs and local lithologies. Red and blue dashed lines denote mixing trajectories between representative PSAs. Gray labels indicate the mixing ratio used to define a hypothetical endmember (e.g., 2:8 denotes an endmember obtained by mixing NMTP and OP in that proportion). Mixing trajectories were calculated using Sr and Nd isotope ratios and elemental concentrations of the respective endmembers (see Methods). For the NMTP, Sr and Nd concentrations were taken from the Taklimakan Desert (TK) sand data (ref. 67).

samples shift toward values around +15%, indicating distinct source contributions compared with the Central Yakutia samples.

The main +10‰ peaks of the measured  $\delta^{18}$ O values in Fig. 4 are attributed to the local influx of granitic or metamorphic components. The Batagay sampling site is located in the Yana River basin along the



**Fig. 4** | **Distribution of δ**<sup>18</sup>**O values for quartz grains across four size fractions at Batagay, Cyuie, and Churapcha. a** > 125 μm. **b** 63–125 μm. **c** 32–63 μm. **d** <32 μm. Raw data are provided in Supplementary Data 4. Distributions are shown as Gaussian kernel density estimates (KDEs; see Methods). Statistical tests (Welch ttest, Mann–Whitney U test, permutation test) indicate highly significant differences between the Batagay and Central Yakutia (Cyuie and Churapcha) distributions across all size fractions (p < 0.001), whereas no significant differences were detected between the Cyuie and Churapcha samples (p ≈ 0.8). The blue-shaded band marks a peak range primarily attributable to local sources, whereas the yellow-shaded band represents a peak range that may reflect contributions from both local sources and long-range transported (LRT) dust originating from the Chinese arid regions. Outlined fields indicate the δ<sup>18</sup>O ranges from the Ordos Plateau to the northern margin of the Tibetan Plateau (OP-NMTP; orange dashed) and those of the Mongolian Gobi (MG; brown dashed), from ref. 27, illustrating overlaps with peaks observed in the samples.

Verkhoyansk Range, where granitoid intrusions are common in the central part of the Verkhoyansk-Kolyma orogen (Supplementary Fig. 1; ref. 39). Through glacial erosion or river discharge, sediments from the Verkhoyansk Mountains could contain significant amounts of quartz grains with  $\delta^{18}$ O values of approximately +10‰, which may have been generated by weathering of granitoid intrusions. Similarly, in the Lena and Aldan River basins, where the Cyuie and Churapcha sampling sites are located, glaciogenic sediments and morainic materials from the

Verkhoyansk Mountains during the Pleistocene are common<sup>40</sup>. Besides, the Lena River flows from the southern part of the Siberian Platform consisting of Proterozoic metamorphic rocks and granitoids<sup>41</sup>, and the Aldan River originates in the Aldan Shield which comprises Archaean metamorphic series<sup>40</sup>. Therefore, the primary sources of Lena and Aldan Rivers are crystalline rocks of metamorphic origins, may comprising the  $\delta^{18}\text{O}$  values of +10%, which is also consistent with the radiogenic  $^{87}\text{Sr}/^{86}\text{Sr}$  and  $\epsilon_{Nd}(0)$  signatures observed in the Central Yakutia samples.

The different peaks of  $\delta^{18}$ O values in the sedimentary component range of approximately +15% seen in Fig. 4 could be contributed by both local sources and LRT dust. The basement of central and northern Yakutia is mostly Mesozoic sedimentary rocks and Late Paleozoic and Mesozoic folded sediments, respectively (Supplementary Fig. 1; ref. 40). Either glacial erosion of local bedrock or aeolian transport like saltation from local sediments can provide a basis for  $\delta^{18}$ O values near +15%. The sedimentary components also likely contain LRT quartz from the Chinese arid regions, as previously suggested by REE and Sr-Nd isotope systematics. In this regard, the ranges of  $\delta^{18}$ O values taking into account particle sizes from the MG  $(+15.1 \text{ to } 17.3\% \text{ for } < 16 \mu\text{m}; +12.6 \text{ to } 15.1\% \text{ for } 16-63 \mu\text{m})$  and the OP and NMTP (+16.1 to 18.5% for <16 μm; +14.0 to 17.0% for 16-63 μm) as reported in ref. 27 overlap with the range in which peaks for sedimentary components appear in the samples. Notably, the  $\delta^{18}O$ distribution of the Batagay samples has a prominent peak in this range (Fig. 4), suggesting that LRT dust may have contributed particularly significantly from the Chinese arid regions to Batagay during the mid-late MIS 3. In addition, for the Batagay samples, the dominant  $\delta^{18}$ O peak near +15% is more pronounced in the finer fractions of quartz particles than in the coarser fractions (Fig. 4d). This may reflect a larger proportion of LRT dust in the finer fractions. The contrasting proportions of +15% peaks between the Batagay and Central Yakutia samples likely reflect different contributions of LRT versus local material, with the Batagay distribution showing a stronger LRT component and the Central Yakutia distributions retaining more local input, consistent with the stronger local signatures in the Central Yakutia samples inferred from REE ratios (Fig. 2) and Sr-Nd isotopes (Fig. 3).

# Discussion

Local sediment accumulation in Yedoma deposits primarily occurred when the surface was unfrozen, relatively dry, and exposed to aeolian processes <sup>11,13</sup>. Accordingly, a large portion of the Yedoma sediments in this region is interpreted as aeolian in origin, although there is no consensus on this and other interpretations exist regarding their origin and deposition processes, especially for sites further north<sup>16,42</sup>. At the Batagay site, sediment transport was mainly through saltation from the surrounding Verkhoyansk Mountains<sup>43</sup>, whereas the Central Yakutia site received sediment primarily via deflation from the Lena-Aldan river plain<sup>40</sup>. Compared to the relatively warm mid-late MIS 3 period, the extremely cold and dry climate of the LGM (MIS 2) likely enhanced deflation, thereby promoting greater local loess accumulation. This likely resulted in a stronger influx of local material in Central Yakutia during the LGM, thereby diminishing the relative contribution of LRT dust in the geochemical signals.

The presence of LRT dust within ice wedges reflects the synoptic-scale atmospheric circulation. Modern climatology offers useful analogues: episodic transport of East Asian dust to the Arctic across Siberia has been observed, particularly via meridional pathways associated with low-pressure systems over northern Japan in spring 44,45. In such cases, dust originating from the Gobi-Taklimakan region is lofted by spring cold-surge fronts into the midtroposphere and couples with the enhanced cyclonic flow over Northeast Asia. Case studies integrating satellite observations, ground-based lidar, trajectory modeling, and reanalysis data

demonstrate that dust storms can follow a meridional shortcut over the Korean Peninsula and Japan, traverse eastern Siberia within days, and deposit even coarse ( $10-50\,\mu m$ ) particles in the Arctic 44,45. A similar mechanism may have been operated during the Late Pleistocene, particularly under the relatively warmer and climatically more variable conditions of the mid-late MIS 3, when the Batagay ice wedges formed.

The enhanced LRT dust signal observed in the Batagay ice wedge samples (mid-late MIS 3) likely reflects synoptic-scale atmospheric circulation. Previous studies have shown that this period was characterized by frequent millennial-scale climate oscillations, which likely influenced atmospheric circulation and dust fluxes<sup>46-49</sup>. However, the temporal resolution of our samples does not allow us to resolve individual millennial-scale events or seasonal variations. Nevertheless, the consistent geochemical similarities with the Chinese aeolian deposits across samples of different ages suggest that episodic meridional dust transport toward East Siberia occurred repeatedly throughout the mid-late MIS 3, regardless of millennial-scale variability. We therefore suggest that the Batagay ice wedges may record evidence of such recurrent transport events facilitated by synoptic-scale circulation before the LGM (Fig. 1; Supplementary Fig. 7a).

In contrast, the Central Yakutia samples (LGM; MIS 2) exhibit a stronger local geochemical signature, despite model simulations indicating elevated atmospheric dust concentrations and strong dust emissions in China during the LGM<sup>9,50</sup>. Paleoclimate simulations suggest a 5-8° southward displacement of the upper-level westerly jet core over the Gobi-Taklimakan, paired with intensified spring uplift driven by a strengthened Siberian High 51,52. A stronger Siberian High and a more zonally confined, southward-shifted westerly wind likely suppressed meridional transport pathways, thereby reducing the delivery of Asian dust to East Siberia (Fig. 1; Supplementary Fig. 7b). At the same time, extremely cold and arid conditions promoted local deflation, further enhancing the contribution of regional sediments. The reduced frequency of meridional transport events, combined with enhanced local sediment input, explains both the weakened LRT dust signals and the stronger local signals observed in the Central Yakutia ice wedges.

Situated along potential meridional transport routes between East Asian deserts and the Arctic, the Yedoma region offers a valuable archive of Late Pleistocene dust activity and atmospheric circulation. Syngenetic ice wedges are particularly suited for this purpose, as they can trap particles directly from the atmosphere and preserve shortterm signals with minimal reworking. By integrating geochemical analyses with modern analogues and paleoclimate models, we suggest that East Siberian Yedoma ice wedges record variations in dust transport pathways during the Late Pleistocene. While our framework links dust provenance shifts to atmospheric circulation variability, it is currently constrained by limited model experiments and available observational records. To address these uncertainties, future work should prioritize higher temporal resolution records from additional Yedoma sites, together with multi-seasonal model simulations and broader regional comparisons. Such efforts will provide valuable insights into dust-climate interactions and their role in shaping Arctic paleoenvironments.

# **Methods**

#### **Pretreatment**

Bulk ice wedge samples were melted and oven-dried at about 40 °C to extract only sediment fractions. The extracted sediment samples were sequentially pretreated with 1 M HCl and 17.5%  $\rm H_2O_2$  to remove acid-soluble minerals (e.g., carbonates) and organic matter, respectively. After the sample settled from the suspension, the supernatant was removed by pipette and 17.5%  $\rm H_2O_2$  solution was added again until all organic material was removed. The resulting inorganic residue was

rinsed three times with Milli-Q water and oven-dried at approximately 60 °C. Each sample was divided into four portions for analyses of particle size distribution, trace elements, and radiogenic and oxygen isotopes.

#### Grain-size distribution

After removing acid-soluble minerals and organic materials, samples were dispersed in distilled water for particle size analysis. Measurements were performed using Mastersizer 3000 Particle Size Analyzer (Malvern Panalytical) at the Cooperative Laboratory Center, Pukyong National University, Republic of Korea. Based on laser diffraction technique, this instrument has a measurement range of 0.01 to 3500  $\mu m$  with 100 size classes. The grain-size distributions were calculated by the Mie scattering theory.

#### Trace element analyses

Trace element concentrations were analyzed for several grain-size fractions (bulk, <125 μm, 63–125 μm, <63 μm, 32–63 μm, and <32 μm) obtained by dry sieving, when sufficient sample material was available. Approximately 0.1g of each sample was weighed and dissolved in a mixture of 5 ml HF, 4 ml HNO<sub>3</sub>, and 1 ml HClO<sub>4</sub> in Teflon digestion vessels at 185 °C for 24 h. After complete dissolution, the decomposed samples were evaporated to dryness on a hot plate, re-dissolved in 3% HNO<sub>3</sub>, and diluted appropriately depending on the target elements. REE and trace element concentrations were determined using an iCAP Q (Thermo Fisher Scientific) inductively coupled plasma mass spectrometer (ICP-MS) at the Korea Institute of Ocean Science and Technology (KIOST), Republic of Korea. Two certified reference materials (CRMs) MESS-4 (marine sediment) and BCR-667 (estuarine sediment) were analyzed alongside the samples to validate the accuracy. The results for the CRMs are summarized in Supplementary Table 3. For MESS-4, recoveries of certified elements are within 11% of the certified values, with relative standard deviations (RSDs) below 8.2%. For BCR-667, recoveries of certified elements are within 8.9% of the certified values, with RSDs below 1.9%.

## Sr and Nd isotope analyses

Sr and Nd isotope analyses were conducted on nine bulk samples, three <10 µm fractions, and three <5 µm fractions using a TRITON plus (Thermo Fisher Scientific) thermal ionization mass spectrometer (TIMS) at Korea Polar Research Institute (KOPRI), Republic of Korea. The <10 µm and <5 µm fractions were separated by gravity sedimentation based on Stokes' Law and subsequently recovered by centrifugation. Approximately 30 mg of each sample was dissolved in a mixture of 2 ml HF, 1 ml HNO<sub>3</sub> and 0.1 ml HClO<sub>4</sub> in closed Teflon vials at 120 °C for 3 to 4 days. Sr was separated using quartz columns (AG 50W-X8, #100-200) with 2.5 N HCl and 6 N HCl and then loaded onto Re filaments with 1M H<sub>3</sub>PO<sub>4</sub>. Nd was extracted by quartz columns (AG 50W-X8, #200-400) using DIW and 0.2 M HIBA (α-Hydroxyisobutyric acid) solution, and loaded onto Re filaments with 0.1 M H<sub>3</sub>PO<sub>4</sub>. For the bulk samples, procedural blanks were <110 pg for Sr and <60 pg for Nd. Reproducibility and accuracy were assessed by analyzing the international reference materials NBS-987 for Sr and JNdi-1 for Nd, which were treated as unknowns. Long-term measurements yielded mean values of  ${}^{87}\text{Sr}/{}^{86}\text{Sr} = 0.710256 \pm 0.000006$  (2 $\sigma$ , n = 15) for NBS-987 and  $^{143}$ Nd/ $^{144}$ Nd = 0.512122 ± 0.000005 (2 $\sigma$ , n = 15) for JNdi-1. Mass fractionation during measurement was corrected by internal normalization to  ${}^{86}\text{Sr}/{}^{88}\text{Sr} = 0.1194$  and  ${}^{146}\text{Nd}/{}^{144}\text{Nd} = 0.7219$ , respectively. During the analyses of fine fractions (<10 and <5 µm), procedural blanks were <41 pg for Sr and <43 pg for Nd. Repeated measurements yielded mean values of  ${}^{87}\text{Sr}/{}^{86}\text{Sr} = 0.710252 \pm 0.000006 \ (2\sigma, n = 8)$  for NBS-987 and  $^{143}$ Nd/ $^{144}$ Nd = 0.512119 ± 0.000004 (2 $\sigma$ , n = 8) for JNdi-1. Each Sr analysis consisted of 100 measurement cycles per run, and each Nd analysis consisted of 140 cycles per run.

#### Oxygen isotope analysis for quartz

To measure oxygen isotopic composition of quartz grains, the samples reacted with a mixture of concentrated  $\rm H_2SiF_6$  and 10% HCl until all clay mineral was removed and only quartz grains remained. Each sample was divided into four size fractions (>125, 63–125, 32–63 and <32  $\mu m$ ) by dry sieving. Quartz grains of >125, 63–125 and 32–63  $\mu m$  fractions were individually hand-picked, mounted in 1-inch epoxy and polished. Due to difficulties in sample preparation, one representative sample from each site was selected to measure the finest fractions. The finest fractions (<32  $\mu m$ ) were mounted in 6-mm diameter acrylic resin to achieve greater flatness during polishing. NBS-28 standards were also prepared with 6-mm diameter resin mount in the same way. The polished acrylic resin mounts were embedded in an indium-filled 1-inch Al disc for higher electrical conductivity. The sample and standard mounts were embedded in the same disc, allowing measurement in the same session. All sample mounts were finally coated with gold prior to measurements.

Oxygen isotope compositions of individual quartz grains were determined by a CAMECA IMS 1300-HR<sup>3</sup> multicollector-equipped ion microprobe at Korea Basic Science Institute (KBSI), Republic of Korea. For the analysis of the coarser grains (>32 μm), a 20 μm Cs<sup>+</sup> primary beam of 2.5 to 3.0 nA accelerated at 10 kV. A 10 keV electron gun of 150 µm in diameter was applied for electrostatic charge compensation. Negative secondary ions were extracted with a potential of -10 kV. The field aperture size was 3000 x 3000 µm. A mass resolving power (MRP) was ~5000 at 10% peak height. Both <sup>16</sup>O and <sup>18</sup>O were simultaneously collected in two Faraday cup detectors fitted with  $10^{10} \Omega$  (L'2) and  $10^{11} \Omega$  (H'2) resistors, respectively. Each analysis consisted of presputtering (80 to 100 s), automatic beam centering to the field and contrast apertures, mass calibration for <sup>16</sup>O, and measurements (20 cycles of 4 s). The instrumental mass fractionation (IMF) was corrected using NBS-28 quartz ( $\delta^{18}O_{V-SMOW} = 9.6\%$ ). Under these conditions, the <sup>16</sup>O' count rate was typically ~1×10<sup>9</sup>cps/nA. An internal precision (standard error of the mean of the cycles in a single measurement; 20) of  $\pm 0.1$  to 0.2% is achieved by NBS-28 quartz standards. The external reproducibility (standard deviation between several spots) was about ±0.3%.

The finest fractions (<32  $\mu$ m) were also measured by in-situ spot analysis, with a 5  $\mu$ m Cs $^+$  beam of ~100 pA.  $^{16}$ O and  $^{18}$ O were detected with a Faraday cup and electron multiplier, respectively. Each analysis consisted of pre-sputtering (80 to 100 s), automatic beam centering, mass calibration, and measurements (20 cycles of 4 s). Other instrumental operation parameters were the same as the analyses of the three coarser fractions (>32  $\mu$ m). Under these conditions, the  $^{16}$ O count rate was typically ~1 × 10 $^8$  cps/nA. The internal precision (2 $\sigma$ ) was  $\pm$ 0.3 to 0.4% by NBS-28 quartz standards. The external reproducibility was about  $\pm$ 0.4‰.

#### Radiocarbon age dating

After melting of ice wedge samples, we freeze-dried the samples and screened the sediments originally included in the wedge ice using a stereo microscope. Organic macro remains were picked. Radiocarbon dating was performed at the MICADAS facility at Alfred Wegener Institute (AWI) Bremerhaven, Germany<sup>53</sup>. Plant remains were cleaned with acid-base-acid treatment as described in ref. 53. The samples were subsequently combusted in an elemental analyzer (Elementar vario Isotope). Produced CO<sub>2</sub> was further graphitized utilizing the automated graphitization system (AGE-3; Ionplus AG; ref. 54) and radiocarbon measurements were conducted. Radiocarbon data were normalized and blank corrected against size-matched standard (NIST Oxalic Acid II, NIST SRM4990C) and <sup>14</sup>C-free blank material (Phthalic Acid; Sigma Aldrich 320064), and data integrity was checked against the processing wood standard IAEA-C5 and lab-internal sediment standards.

All radiocarbon results were reported as F<sup>IA</sup>C and conventional radiocarbon ages (Supplementary Table 2). We used the IntCal20 dataset (ref. 55) to calibrate the ages with CALIB Radiocarbon Calibration version 8.2 (ref. 56), which are given as calibrated years before present (cal yr BP). We also calibrated non-finite ages for comparative reasons. To provide a minimum age estimate, a theoretical standard deviation of 1000 radiocarbon years was computed in CALIB following ref. 57. We have rounded all results with standard deviations in the radiocarbon ages greater than 50 yr to the nearest 10 yr.

#### Calculation for Sr-Nd mixing curves

Binary mixing trajectories in Fig. 3 between PSA endmembers were calculated using average Sr and Nd isotope ratios and elemental concentrations of the respective endmembers. The mixed isotopic ratio  $R_{\rm mix}$  was obtained as:

$$R_{\text{mix}} = \frac{f_A C_A R_A + f_B C_B R_B}{f_A C_A + f_B C_B} \tag{1}$$

where *R* is the isotope ratio, *C* is the element concentration (Sr or Nd), and f is the mixing fraction of endmembers *A* and *B*.

#### Oxygen isotope distributions

The  $\delta^{18}$ O distributions of quartz grains were evaluated using Gaussian kernel density estimation (KDE) with bandwidth h determined by the normal reference rule ( $h = \sigma \cdot (4/(3n))^{1/5}$ ), where  $\sigma$  is the standard deviation and n is the number of measurements; ref. 58). KDEs were calculated using Microsoft Excel (Microsoft Ltd., USA) with the Real Statistics Resource Pack (Release 8.9.1; ref. 59). Group differences were assessed for each size fraction (>125, 63–125, 32–63, and <32  $\mu$ m) using three statistical approaches: Welch t-test, Mann–Whitney U test, and permutation test.

#### **Ice-sheet reconstructions**

To illustrate the ice-sheet extent in Fig. 1, we used published reconstructions of the Eurasian Ice Sheet Complex (EISC), Greenland Ice Sheet (GIS), Laurentide Ice Sheet (LIS), and Cordilleran Ice Sheet (CIS) from refs. 60,61. Within the MIS 3 reconstructions, only the 40 ka time slice shows a more extensive ice cover in eastern Siberia because it incorporates a maximum Quaternary ice-extent template to match empirical evidence from the Kamchatka Peninsula<sup>60</sup>. This likely overestimates the ice extent in the Verkhoyansk region, where field evidence indicates limited local glaciation<sup>62-64</sup>. To avoid misinterpretation, the 40 ka reconstruction was excluded, and the MIS 3 ice extent is illustrated using the 30, 35, and 45 ka time slices.

#### Data availability

All data generated in this study are provided in the Supplementary Information and the Source Data files.

#### References

- Aléon, J., Chaussidon, M., Marty, B., Schütz, L. & Jaenicke, R. Oxygen isotopes in single micrometer-sized quartz grains: tracing the source of Saharan dust over long-distance atmospheric transport. Geochim. Cosmochim. Acta 66, 3351–3365 (2002).
- 2. Pye, K. Aeolian dust and dust deposits (Elsevier, 2015).
- Sun, J. Provenance of loess material and formation of loess deposits on the Chinese Loess Plateau. Earth Planet. Sci. Lett. 203, 845–859 (2002).
- Schütz, L., Jaenicke, R. & Pietrek, H. Saharan dust transport over the North Atlantic Ocean. Geol. Soc. Am. Bull. Spec. Pap. 186, 87 (1981).
- Nagashima, K. et al. Millennial-scale oscillations of the westerly jet path during the last glacial period. J. Asian Earth Sci. 40, 1214–1220 (2011).

- Miller, R. & Tegen, I. Climate response to soil dust aerosols. J. Clim. 11. 3247–3267 (1998).
- Sassen, K., DeMott, P. J., Prospero, J. M. & Poellot, M. R. Saharan dust storms and indirect aerosol effects on clouds: CRYSTAL-FACE results. Geophys. Res. Lett. 30, 1633 (2003).
- 8. Lambert, F. et al. The role of mineral-dust aerosols in polar temperature amplification. *Nat. Clim. Change* **3**, 487–491 (2013).
- Mahowald, N. M. et al. Change in atmospheric mineral aerosols in response to climate: last glacial period, preindustrial, modern, and doubled carbon dioxide climates. J. Geophys. Res. Atmos. 111, D10202 (2006).
- Albani, S. et al. Aerosol-climate interactions during the last glacial maximum. Curr. Clim. Change Rep. 4, 99–114 (2018).
- Murton, J. B. et al. Palaeoenvironmental interpretation of Yedoma silt (Ice Complex) deposition as cold-climate loess, Duvanny Yar, northeast Siberia. *Permafr. Periglac. Process.* 26, 208–288 (2015).
- 12. Sun, D. et al. Bimodal grain-size distribution of Chinese loess, and its palaeoclimatic implications. *Catena* **55**, 325–340 (2004).
- Péwé, T. L. & Journaux, A. Origin and character of loesslike silt in unglaciated south-central Yakutia, Siberia, USSR. Rep. No. 2330-7102 (USGPO, 1983).
- 14. Li, Y., Shi, W., Aydin, A., Beroya-Eitner, M. A. & Gao, G. Loess genesis and worldwide distribution. *Earth Sci. Rev.* **201**, 102947 (2020).
- Kanevskiy, M., Shur, Y., Fortier, D., Jorgenson, M. & Stephani, E. Cryostratigraphy of late Pleistocene syngenetic permafrost (yedoma) in northern Alaska, Itkillik River exposure. Quat. Res. 75, 584–596 (2011).
- Schirrmeister, L., Froese, D., Tumskoy, V., Grosse, G. & Wetterich, S. Yedoma: Late Pleistocene ice-rich syngenetic permafrost of Beringia. *Encycl. Quat. Sci.* 3, 542–552 (2013).
- 17. Pewe, T. L. Origin of the upland silt near Fairbanks, Alaska. Geol. Soc. Am. Bull. **66**, 699–724 (1955).
- Opel, T. et al. Ice wedges as archives of winter paleoclimate: a review. Permafr. Periglac. Process. 29, 199–209 (2018).
- Kanevskiy, M. et al. Cryostratigraphy and Permafrost Evolution in the Lacustrine Lowlands of West-Central Alaska. *Permafr. Periglac. Process.* 25, 14–34 (2014).
- Nitzbon, J. et al. Fast response of cold ice-rich permafrost in northeast Siberia to a warming climate. Nat. Commun. 11, 2201 (2020).
- Kim, K. et al. Greenhouse gas formation in ice wedges at Cyuie, central Yakutia. Permafr. Periglac. Process. 30, 48–57 (2019).
- 22. Yang, J. W. et al. Origin of CO<sub>2</sub>, CH<sub>4</sub>, and N<sub>2</sub>O trapped in ice wedges in central Yakutia and their relationship. *Permafr. Periglac. Process.* **34**, 122–141 (2023).
- 23. Park, H. et al. A biogeochemical study of greenhouse gas formation from two ice complexes of Batagay Megaslump, East Siberia. *Permafr. Periglac. Process.* **35**, 437–449 (2024).
- 24. Murton, J. B. et al. A multimethod dating study of ancient permafrost, Batagay Megaslump, east Siberia. Quat. Res. 105, 1–22 (2022).
- Ferrat, M. et al. Improved provenance tracing of Asian dust sources using rare earth elements and selected trace elements for palaeomonsoon studies on the eastern Tibetan Plateau. Geochim. Cosmochim. Acta 75, 6374–6399 (2011).
- Grousset, F. E. & Biscaye, P. E. Tracing dust sources and transport patterns using Sr, Nd and Pb isotopes. *Chem. Geol.* 222, 149–167 (2005).
- Yan, Y., Sun, Y., Chen, H. & Ma, L. Oxygen isotope signatures of quartz from major Asian dust sources: implications for changes in the provenance of Chinese loess. *Geochim. Cosmochim. Acta* 139, 399–410 (2014).
- Vandenberghe, J. Grain size of fine-grained windblown sediment: A powerful proxy for process identification. *Earth Sci. Rev.* 121, 18–30 (2013).

- Clayton, R., Rex, R., Syers, J. & Jackson, M. Oxygen isotope abundance in quartz from Pacific pelagic sediments. J. Geophys. Res. 77, 3907–3915 (1972).
- 30. Taylor, S. R. & McLennan, S. M. The continental crust: its composition and evolution (Blackwell, 1985).
- Biscaye, P. E. et al. Asian provenance of glacial dust (stage 2) in the Greenland Ice Sheet Project 2 Ice Core, Summit, Greenland. J. Geophys. Res. Oceans 102, 26765–26781 (1997).
- Svensson, A., Biscaye, P. E. & Grousset, F. E. Characterization of late glacial continental dust in the Greenland Ice Core Project ice core. J. Geophys. Res. Atmos. 105, 4637–4656 (2000).
- Bory, A. J. M., Biscaye, P. E. & Grousset, F. E. Two distinct seasonal Asian source regions for mineral dust deposited in Greenland (NorthGRIP). Geophys. Res. Lett. 30, 1167 (2003).
- Újvári, G. et al. Two possible source regions for central Greenland last glacial dust. Geophys. Res. Lett. 42, 10399-10408 (2015).
- Gaiero, D. M. Dust provenance in Antarctic ice during glacial periods: From where in southern South America?. Geophys. Res. Lett. 34, L17707 (2007).
- Rachold, V., Eisenhauer, A., Hubberten, H.-W., Hansen, B. & Meyer, H. Sr isotopic composition of suspended particulate material (SPM) of East Siberian Rivers: Sediment transport to the Arctic Ocean. Arc. Alp. Res. 29, 422–429 (1997).
- 37. Astakhov, A. S. et al. Distribution and sources of rare earth elements in sediments of the Chukchi and East Siberian Seas. *Polar Sci.* **20**, 148–159 (2019).
- 38. Rachold, V. Land-ocean systems in the Siberian Arctic: Dynamics and history (Springer, 1999).
- Oxman, V. S. Tectonic evolution of the Mesozoic Verkhoyansk–Kolyma belt (NE Asia). Tectonophysics 365, 45–76 (2003).
- 40. Popp, S. Late quaternary environment of Central Yakutia (NE Siberia): signals in frozen ground and terrestrial sediments. *Ber. Polar-Meerforsch.* **554**, 80 (2007).
- Dolginow, E., Kropatschjow, S. & Klitzsch, E. Abriß der Geologie Rußlands und angrenzender Staaten (E. Schweizerbart'sche Verlagsbuchhandlung, 1994).
- Schirrmeister, L. et al. Sedimentary characteristics and origin of the Late Pleistocene Ice Complex on north-east Siberian Arctic coastal lowlands and islands-A review. Quat. Int. 241, 3-25 (2011).
- 43. Murton, J. B. et al. Preliminary paleoenvironmental analysis of permafrost deposits at Batagaika Megaslump, Yana Uplands, northeast Siberia. *Quat. Res.* **87**, 314–330 (2017).
- 44. Zhao, X., Huang, K., Fu, J. S. & Abdullaev, S. F. Long-range transport of Asian dust to the Arctic: identification of transport pathways, evolution of aerosol optical properties, and impact assessment on surface albedo changes. Atmos. Chem. Phys. 22, 10389–10407 (2022).
- 45. Huang, Z. et al. Short-cut transport path for Asian dust directly to the Arctic: a case study. *Environ. Res. Lett.* **10**, 114018 (2015).
- Újvári, G. et al. Coupled European and Greenland last glacial dust activity driven by North Atlantic climate. *Proc. Natl Acad. Sci. USA* 114, E10632–E10638 (2017).
- 47. Újvári, G., et al. Greenland ice core record of last glacial dust sources and atmospheric circulation. *J. Geophys. Res. Atmos.* **127**, e2022JD036597 (2022).
- Steffensen, J. P. The size distribution of microparticles from selected segments of the Greenland Ice Core Project ice core representing different climatic periods. J. Geophys. Res. Oceans 102, 26755–26763 (1997).
- Ruth, U., Wagenbach, D., Steffensen, J. P. & Bigler, M. Continuous record of microparticle concentration and size distribution in the central Greenland NGRIP ice core during the last glacial period. J. Geophys. Res. Atmos. 108, 4098 (2003).

- 50. Mahowald, N. et al. Dust sources and deposition during the last glacial maximum and current climate: a comparison of model results with paleodata from ice cores and marine sediments. *J. Geophys. Res. Atmos.* **104**, 15895–15916 (1999).
- Brady, E. C., Otto-Bliesner, B. L., Kay, J. E. & Rosenbloom, N. Sensitivity to glacial forcing in the CCSM4. *J. Clim.* 26, 1901–1925 (2013).
- 52. Yanase, W. & Abe-Ouchi, A. The LGM surface climate and atmospheric circulation over East Asia and the North Pacific in the PMIP2 coupled model simulations. *Clim* **3**, 439–451 (2007).
- Mollenhauer, G., Grotheer, H., Gentz, T., Bonk, E. & Hefter, J. Standard operation procedures and performance of the MICADAS radiocarbon laboratory at Alfred Wegener Institute (AWI), Germany. Nucl. Instrum. Meth. B 496, 45–51 (2021).
- 54. Wacker, L., Němec, M. & Bourquin, J. A revolutionary graphitisation system: fully automated, compact and simple. *Nucl. Instrum. Meth. B* **268**, 931–934 (2010).
- Reimer, P. J. et al. The IntCal20 Northern Hemisphere radiocarbon age calibration curve (0-55 cal kBP). *Radiocarbon* 62, 725–757 (2020).
- Stuiver, M. & Reimer, P. J. Extended 14C data base and revised CALIB 3.0 14C age calibration program. *Radiocarbon* 35, 215–230 (1993).
- 57. Leder, D. et al. A 51,000-year-old engraved bone reveals Nean-derthals' capacity for symbolic behaviour. *Nat. Ecol. Evol.* **5**, 1273–1282 (2021).
- 58. Silverman, B. W. Density estimation for statistics and data analysis (Routledge, 2018).
- Zaiontz, C. Real Statistics resource pack. Real Statistics using Excel. http://www.real-statistics.com (2021).
- Batchelor, C. L. et al. The configuration of Northern Hemisphere ice sheets through the Quaternary. Nat. Commun. 10, 3713 (2019).
- Batchelor, C. L., Krapp, M., Manica, A. & Murton, D. K. The configuration of Northern Hemisphere ice sheets through the Quaternary. https://doi.org/10.17605/OSF.IO/7JEN3 (2025).
- 62. Stauch, G. & Lehmkuhl, F. Quaternary glaciations in the Verkhoyansk Mountains, northeast Siberia. *Quat. Res.* **74**, 145–155 (2010).
- 63. Stauch, G. & Gualtieri, L. Late Quaternary glaciations in north-eastern Russia. J. Quat. Sci. 23, 545–558 (2008).
- 64. Diekmann, B. et al. Late Quaternary lake dynamics in the Verkhoyansk Mountains of Eastern Siberia: implications for climate and glaciation history. *Polarforsch* **86**, 97–110 (2017).
- 65. Strauss, J. et al. Circum-Arctic map of the Yedoma permafrost domain. *Front. Earth Sci.* **9**, 758360 (2021).
- 66. Strauss, J. et al. Database of Ice-Rich Yedoma Permafrost Version 2 (IRYP v2). https://doi.org/10.1594/PANGAEA.940078 (2022).
- 67. Yang, X., Zhu, B. & White, P. D. Provenance of aeolian sediment in the Taklamakan Desert of western China, inferred from REE and major-elemental data. *Quat. Int.* **175**, 71–85 (2007).

#### Acknowledgements

This research was supported by the R&D Program for Oceans and Polar Regions of the National Research Foundation (NRF) funded by the Ministry of Science and ICT (RS-2020-NR045823). J.K. and Y.L. were supported by the Korea Basic Science Institute grant (C511000). M.J.L. was financially sponsored by the Ministry of Oceans and Fisheries of Korea (PE25050). T.O. was funded by the Leverhulme Trust under Grant RPG-2020-334 and by the MARUM Cluster of Excellence "The Oceans Floor – Earth's Uncharted Interface" (German Research Foundation DFG, Project number 390741603). We thank Kwangjin Yim, Sarang Choi, Seolhui Bang, and Hyeonjeong Jeong for preparing samples. We are grateful to Kongtae Ra and Seung Hee Han for helping analyses of trace elements and radiogenic isotopes, respectively. We would like to thank the staff at the AWI facility MICADAS for their support with the analysis.

#### **Author contributions**

S.K., H.L., and J.A. conceptualized the study. S.K. performed trace element and isotope analysis. J.K., Y.L., and J.-H.C. collaborated on oxygen isotope analysis. M.J.L. collaborated on Sr and Nd isotope analysis. S.K. and U.-J.K. conducted the statistical analysis and interpreted the atmospheric circulation. G.I., T.O., H.M., S.W., and A.F. contributed to securing ice wedge samples. T.O. interpreted radiocarbon age data for the Batagay ice wedges. H.L. and J.A. acquired funding and managed the project. S.K. and H.L. wrote the original manuscript, and all the authors participated in the review and editing.

# **Competing interests**

The authors declare no competing interests.

# **Additional information**

**Supplementary information** The online version contains supplementary material available at https://doi.org/10.1038/s41467-025-65772-2.

**Correspondence** and requests for materials should be addressed to Hyunwoo Lee.

**Peer review information** *Nature Communications* thanks Bess Koffman, Frank Lehmkuhl, and the other, anonymous, reviewer(s) for their contribution to the peer review of this work. A peer review file is available.

**Reprints and permissions information** is available at http://www.nature.com/reprints

**Publisher's note** Springer Nature remains neutral with regard to jurisdictional claims in published maps and institutional affiliations.

Open Access This article is licensed under a Creative Commons Attribution-NonCommercial-NoDerivatives 4.0 International License, which permits any non-commercial use, sharing, distribution and reproduction in any medium or format, as long as you give appropriate credit to the original author(s) and the source, provide a link to the Creative Commons licence, and indicate if you modified the licensed material. You do not have permission under this licence to share adapted material derived from this article or parts of it. The images or other third party material in this article are included in the article's Creative Commons licence, unless indicated otherwise in a credit line to the material. If material is not included in the article's Creative Commons licence and your intended use is not permitted by statutory regulation or exceeds the permitted use, you will need to obtain permission directly from the copyright holder. To view a copy of this licence, visit <a href="https://creativecommons.org/licenses/by-nc-nd/4.0/">https://creativecommons.org/licenses/by-nc-nd/4.0/</a>.

© The Author(s) 2025